Chemical Science

ROYAL SOCIETY OF CHEMISTRY

EDGE ARTICLE

View Article Online
View Journal | View Issue

Cite this: *Chem. Sci.*, 2025, **16**, 17640

All publication charges for this article have been paid for by the Royal Society of Chemistry

Received 24th June 2025
Accepted 21st August 2025

DOI: 10.1039/d5sc04645a

rsc.li/chemical-science

Synergistic Cu-based catalysts with multiple active sites for high-efficiency Li–CO_2 batteries

Shasha Xiao,[a] Ying Xiao,*[a] Gang He,[a] Tonghui Zhang,[a] Longlong Yang,[a] Feng Huo [b] and Shimou Chen *[a]

The lithium-carbon dioxide (Li–CO_2) battery is a promising energy storage technology that integrates CO_2 utilization with energy storage and conversion. However, its development is hindered by slow reaction kinetics and insulating Li_2CO_3 discharge products deposited at the cathode, which cause severe polarization and rapid capacity degradation. Herein, novel Cu-based catalysts with multiple active sites anchored on nitrogen-doped carbon (Cu/NC) are developed to achieve highly efficient Li–CO_2 batteries. Metallic Cu nanoparticles facilitate efficient electron transfer during the CO_2 reduction reaction (CO_2RR), while the induced Cu–N/O dual active sites effectively reduce the energy barrier for decomposing discharge products. Furthermore, the optimized N configurations in the NC matrix enhance the intrinsic activity of the catalytic sites. Consequently, the Li–CO_2 battery incorporating the optimized catalyst demonstrates attractive cycling stability over 850 h at 300 mA g^{-1}, with a remarkably low overpotential of 1.30 V, showing great potential for low-cost and highly efficient Li–CO_2 batteries. This work provides a strategic route for designing cost-effective multi-active-site catalysts, offering critical insights into the development of high-performance Li–CO_2 batteries.

Introduction

With the increasing global demand for energy storage, conventional lithium-ion batteries (*ca.* 350 W h kg^{-1}) are insufficient to meet the requirements of high-tech applications and long-range electric vehicles.[1–3] In this regard, lithium-carbon dioxide (Li–CO_2) batteries have garnered significant attention due to their high theoretical energy density (1876 W h kg^{-1}) and dual capability of CO_2 capture and conversion.[4–7] Despite their promise as next-generation energy storage systems, Li–CO_2 batteries face critical commercialization challenges. On the one hand, in the discharge process, the progressive accumulation of insulating Li_2CO_3 invariably induces cathodic surface passivation, electrical conductivity degradation, and catalytic active site blockage.[8,9] In the recharge process, the thermodynamic stability of Li_2CO_3 necessitates exceptionally high decomposition voltages (typically beyond 4.3 V), resulting in severe side reactions and substantial electrochemical polarization, leading to rapid capacity fade and shortened cycle life.[10–12]

To address these challenges, the development of high-performance cathodic catalysts capable of simultaneously accelerating CO_2 reduction reaction kinetics and promoting Li_2CO_3 decomposition has been regarded as an efficient strategy and has aroused significant research interest in recent years.[13,14] Among all the electrochemical catalysts, transition metal-based catalysts are widely applied in various electrochemical catalytic reactions such as the urea oxidation reaction, CO_2 reduction reaction and hydrogen evolution reaction due to their appealing electronic structure tunability, economic efficiency, and resource abundance.[4,12,15,16] In particular, Cu-based catalysts with a wide range of oxidation states (Cu^0, Cu^I, Cu^{II}, and Cu^{III}) and adjustable electronic structure have attracted enormous interest and exhibited great promise for Li–CO_2 batteries.[17,18] For instance, Xu *et al.*[19] combined Cu polyphthalocyanine with carbon nanotubes to obtain a Cu single-atom catalyst anchored on a conductive porphyrin network, realizing a low polarization of 1.8 V at 2000 mA g^{-1} in Li–CO_2 batteries. By using the solvothermal method, Cu-tetra(4-carboxyphenyl) porphyrin (Cu-TCPP) nanosheets were demonstrated to be an efficient catalyst, which contributed to sustaining 123 cycles at 500 mA g^{-1}. Despite these promising results, Cu-based catalysts still face significant challenges, including slow reaction kinetics, poor selectivity and insufficient stability, and thus require further development.

Inspired by the above-mentioned studies, herein, we developed a novel ultrafine Cu nanoparticle (NP)-decorated nitrogen-doped carbon (Cu/NC) as a high-efficiency catalyst for Li–CO_2 batteries. Comprehensive characterization revealed that metallic Cu nanoparticles facilitate electron transfer during CO_2

[a]*State Key Laboratory of Chemical Resource Engineering, Beijing Key Laboratory of Electrochemical Process and Technology for Materials, National Engineering Research Center for Fuel Cell and Hydrogen Source Technology, Beijing University of Chemical Technology, Beijing 100029, P. R. China. E-mail: yxiao@buct.edu.cn; chensm@buct.edu.cn*

[b]*Longzihu New Energy Laboratory, Henan University, Zhengzhou, 450046, P. R. China*

reduction, while Cu–N/O moieties effectively reduce Li_2CO_3 decomposition barriers. Additionally, N-doped carbon with optimized N configurations contributes to improved catalytic activity. Such attractive structural properties endow the Li–CO_2 battery with an optimized Cu/NC catalyst that delivers a low overpotential of 1.30 V and extended cycling stability over 850 h at 300 mA g^{-1}, exhibiting great prospects as a low-cost catalyst for Li–CO_2 batteries.

Results and discussion

Fig. 1a schematically illustrates the formation process of Cu/NC *via* pyrolysis of a precursor containing melamine, cyanuric acid (CA), and copper(II) nitrate hexahydrate under an Ar atmosphere. Specifically, the precursor was prepared by first mixing an aqueous solution of CA, melamine and copper nitrate to form a copper-containing supramolecular complex owing to the hydrogen bond interaction between them.[20] Subsequently, due to the weakly alkaline nature of the melamine solution, the $-O^-$ groups in CA molecules coordinated with Cu^{2+} ions to form Cu–O bonds,[21] while nitrogen atoms in melamine rings coordinated with Cu^{2+} ions, establishing Cu–N coordination.[20] The XRD analysis of the self-assembled precursor (Fig. S1) revealed two new diffraction peaks at $2\theta = 11°$ and 28° can be detected, which cannot be assigned to a certain product. We infer this may be caused by the periodic arrangements of intraplanar stacking and interlayer aromatic stacking, which demonstrates the well-ordered hydrogen-bonded network within the supramolecular architecture,[22] confirming successful complex formation. The XRD pattern of the precursor of pure NC, which was prepared without copper nitrate, was nearly identical to that of the precursor of Cu/NC, demonstrating that the Cu/NC precursor maintained the structural advantages of the supramolecular template, thereby laying the foundation for the subsequent pyrolysis to prepare highly dispersed Cu/NC catalysts. The Fourier transform infrared (FTIR) spectroscopy data shown in Fig. S2 indicate that the C=O stretching vibrations ($\nu_{C=O}$) for CA appear at 1781 and 1735 cm^{-1} in the Cu/NC precursor, showing an obvious blue shift compared to those in the reported literature (1739 and 1695 cm^{-1}), which may be caused by the formation of hydrogen-bonded supramolecular aggregates through N–H···O and N–H···N hydrogen bonds between melamine and CA.[23,24] Furthermore, the Cu/NC precursor exhibits an FTIR spectrum similar to that of the CN (Cu-free) precursor, implying that Cu^{2+} incorporation does not affect the formation of the hydrogen-bonded supramolecular assembly. Subsequent pyrolysis at 600 °C for 2 hours under an Ar atmosphere contributed to the formation of N-doped carbon and the firm anchoring of the active sites of the Cu–N/O coordination structure, with most Cu atoms evolving into nanoparticles encapsulated by N-doped carbon to form the Cu/NC catalyst (designated m-Cu/NC). Compared to the precursor, new peaks at 3700–3000 and 1800–1100 cm^{-1} have emerged in the FTIR spectra of Cu/NC (Fig. S2), proving the existence of a heterocyclic ring structure.[25] To probe the influence of the Cu-based active sites on the catalytic activity, catalysts with different Cu contents (0.01 M and 0.05 M) were prepared and named s-Cu/NC and l-Cu/NC, respectively.

The morphology of the catalyst was investigated by using the SEM technique first. As shown in Fig. 1b, the as-formed m-Cu/NC displays uniform nanoparticles with an average diameter of 27.9 nm. These ultrafine nanoparticles are beneficial for increasing the surface area, thus providing more catalytic activity sites and accelerating the reaction kinetics.[26] In contrast, s-Cu/NC presents larger irregular particle agglomerates, and l-Cu/NC shows a flower-like morphology formed by the accumulation of both extremely large and small particles (Fig. S3 and S4). This difference may arise from variations in concentrations. At lower concentrations, fewer nucleation sites form, allowing sufficient time for particle growth and facilitating the formation of larger particles. Conversely, at higher concentrations, explosive nucleation rapidly generates numerous small crystal nuclei, and small particles subsequently attach to larger ones.[27] The TEM images (Fig. 1c and d) further confirm the formation of small nanoparticles uniformly distributed in the amorphous carbon layer. The HRTEM images displayed in Fig. 1e and f distinctly confirm the presence of amorphous carbon and the tight coating of Cu nanoparticles by the carbon layer, which are beneficial for enhancing the structural stability of active sites during repeat electrochemical processes and thus contribute to the long lifespan of the batteries.[28,29] The lattice fringes of 0.208 nm and 0.183 nm were identified, corresponding to the (111) and (200) crystal planes of metallic Cu, respectively, confirming the formation of crystalline Cu. Nitrogen adsorption–desorption isotherms were measured at 77 K to characterize the surface area and pore size distribution of the m-Cu/NC sample (Fig. 1g). The presence of a Type IV isotherm with an H3-type hysteresis loop in the high-pressure region confirms the existence of a mesoporous structure,[30] which helps accelerate the CO_2 gas diffusion and Li^+ transport in the electrolyte, thereby reducing concentration polarization and lowering the charge–discharge overpotential.[31] The BET surface area of m-Cu/NC is calculated to be 64.6 m^2 g^{-1} with a dominant diameter of *ca.* 2.58 nm. The larger specific surface area facilitates the exposure of more catalytically active sites, enabling the efficient adsorption of CO_2 reactive species on the external surface active centers and thus enhancing the CO_2 reduction reaction (CO_2RR) performance.[32–34]

Fig. 2a shows the XRD patterns of the prepared samples. The diffraction peaks located at 43.3°, 50.5°, and 74.1° can be well matched with the (111), (200), and (220) crystal planes of cubic phase Cu (JCPDS no. 98-000-0172).[35] No obvious diffraction peaks related to carbon can be detected, which may be overlapped by the sharp diffraction peaks of Cu. Fig. 2b displays the Raman spectra of the three samples, where two peaks appear at 1427 and 1594 cm^{-1}, corresponding to the characterization peaks of the D-band and G-band of carbon, respectively.[36] The D-band is associated with structural defects or edges in the sample, while the G-band corresponds to sp^2-hybridized graphitic carbon.[37] From the I_D/I_G ratio displayed in Fig. 3c, it can be see that the m-Cu/NC sample exhibits the highest I_D/I_G ratio (1.01) compared to its counterparts (0.88 for s-Cu/NC and

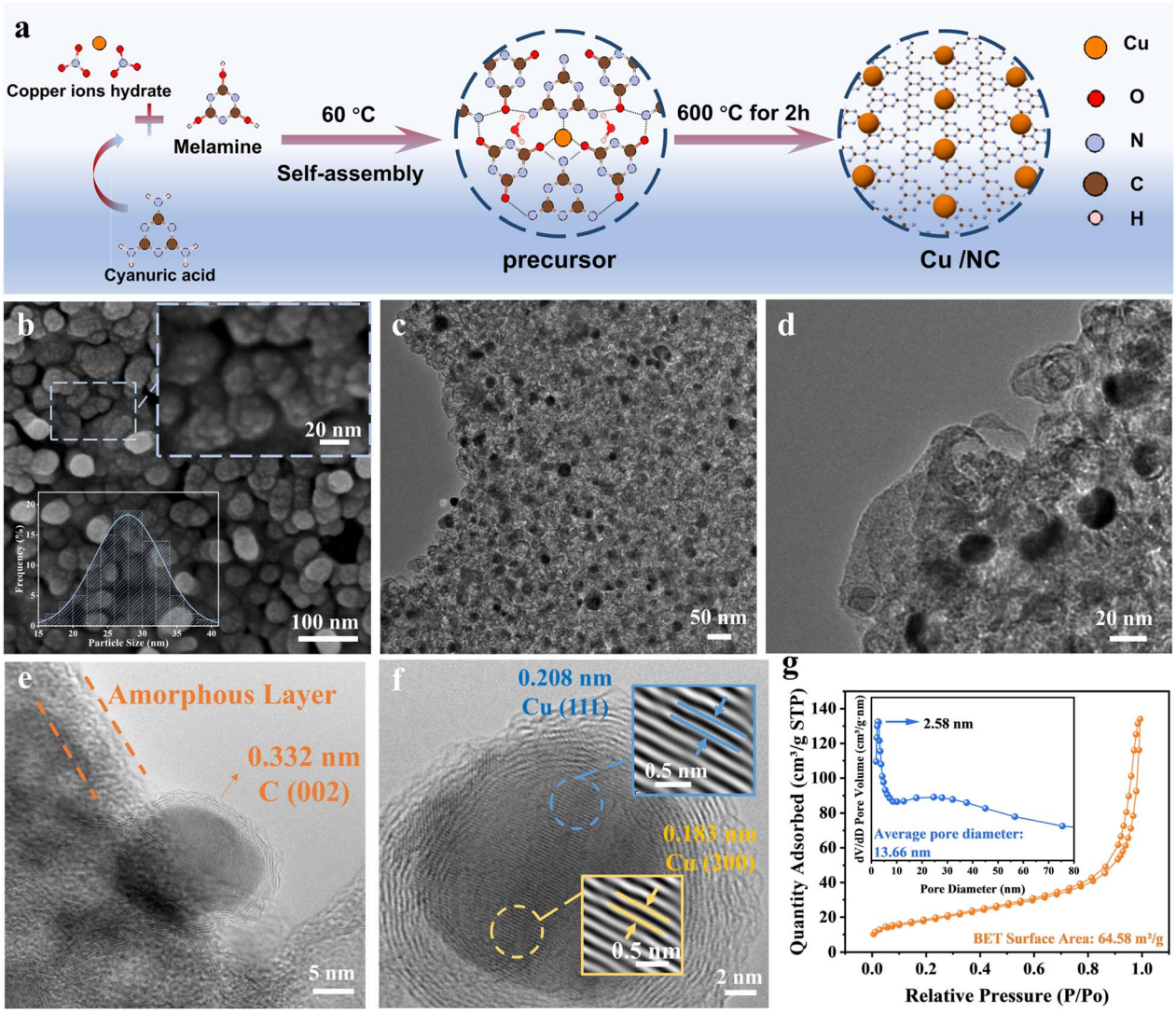

Fig. 1 (a) Schematic illustration of the formation process of Cu/NC. (b) SEM images of m-Cu/NC and the corresponding size distribution of Cu NPs (inset). (c and d) TEM images of m-Cu/NC. (e and f) HRTEM images of m-Cu/NC. (g) N_2 adsorption–desorption isotherms of m-Cu/NC and the related pore size distribution (inset).

0.75 for l-Cu/NC), indicating the formation of more enriched defects, which can serve as active centers that promote the reaction between Li^+ and CO_2, thereby enhancing the CO_2RR performance.[38] Surprisingly, the D-band deviated significantly from the conventional position (1350 cm^{-1}),[39] which may originate from the high-frequency displacement N doping or the interfacial stress between the Cu NPs and carbon matrix, both inducing lattice distortion of the carbon skeleton.[40,41] In addition, one peak appearing at 1290 cm^{-1} can be detected in these three samples, which can be assigned to the stretching vibration of C–N.[42] The FTIR spectra displayed in Fig. 2d confirmed the presence of C=O (1623 cm^{-1}), C–N group (1500–1000 cm^{-1}), Cu–N bond (530 cm^{-1}), and Cu–O stretching modes (437 cm^{-1}).[43–45] To further explore the chemical states and coordination environments in Cu/NC, XPS analysis was systematically performed (Fig. 2f and h). The high-resolution C 1s spectrum (Fig. S5) of m-Cu/NC can be divided into three components: C–C (284.8 eV), C–N (286.6 eV), and C=O (288.5 eV), indicating the formation of N-doped carbon.[46] The peak position of C–N slightly shifts to a higher binding energy compared to that of the standard value (usually *ca.* 285.6 eV),[47–49] which may be caused by the electronic coupling effect of Cu NPs.[50] The N 1s spectrum of m-Cu/NC can be deconvoluted into three peaks at 397.8 eV (16.7 at%), 398.9 eV (72.7 at%), and 400.8 eV (10.6 at%), corresponding to Cu–N, pyridinic-N and pyrrolic N, respectively (Fig. 2f).[51] Meanwhile, the N 1s spectra of s-Cu/NCs and l-Cu/NCs indicate that the formed Cu–N, pyridinic-N and pyrrolic N are present in different percentages (2.5 at%, 67.5 at%, and 30.0 at% for the former and 21.3 at%, 60.4 at%, and 18.3 at% for the latter). Compared with the other samples, the m-Cu/NC exhibits the highest pyridinic-N content (Fig. 2e). According to the literature, pyridinic N can serves as active sites for the oxygen reduction reaction (ORR) by modulating the electronic structure of adjacent carbon atoms and

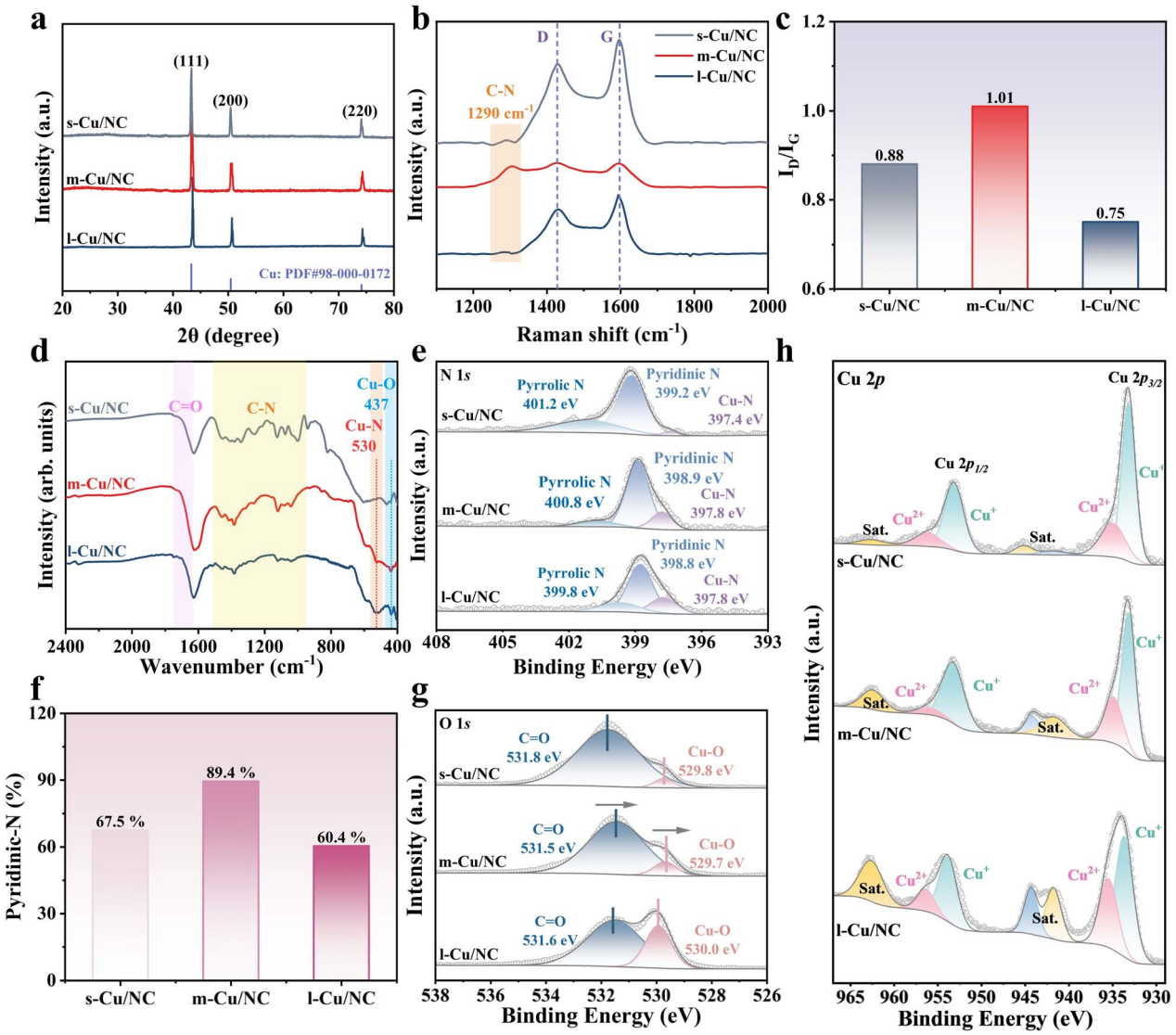

Fig. 2 (a) XRD patterns, (b) Raman spectra, (c) I_D/I_G, (d) FTIR spectra, (e) N 1s XPS spectra, (f) Comparison chart of pyridinic-N content, (g) O 1s XPS spectra and (h) Cu 2p XPS spectra of the three samples.

enhancing charge transfer efficiency, which can provide additional active sites for CO_2 conversion in Li–CO_2 batteries, leading to enhanced electrochemical performance.[52,53] Thus, m-Cu/NC is believed to show attractive electrochemical performance in Li–CO_2 batteries. Furthermore, the O 1s XPS spectrum of m-Cu/NC (Fig. 2g) shows a dominant peak at 531.5 eV related to C=O, and the peak at 529.7 eV corresponds to Cu–O coordination.[33] Meanwhile, Cu 2p XPS spectra (Fig. 2h) displayed characteristic peaks at 933.2/953.4 eV (Cu $2p_{3/2}$ and $2p_{1/2}$ for Cu–N) and 935.0/956.1 eV (corresponding to Cu–O). Satellite peaks at 941.8, 944.3, and 962.7 eV confirmed the Cu^{2+} oxidation state.[54,55] Furthermore, XPS quantitative analysis reveals that the Cu atomic content is 17.29% in m-Cu/NC, compared with 2.91% in s-Cu/NC and 21.37% in l-Cu/NC. The moderate Cu content in m-Cu/NC provides an optimal density of surface active sites, effectively promoting CO_2 reduction for Li_2CO_3 formation during discharge. Notably, insufficient Cu content (as s-Cu/NC) results in limited catalytic activity, while excessive Cu loading (as l-Cu/NC) induces nanoparticle agglomeration, which blocks porous channels and increases the energy barrier for discharge product decomposition, ultimately impairing battery performance.[17] These results conclusively demonstrate the coexistence of dual Cu active centers (Cu–N and Cu–O) in the m-Cu/NC, which can serve as electron transfer channels, optimizing the D-band electron structure of the Cu active center and helping to promote CO_2 reaction activity and enhance reaction kinetics.[56]

Electrochemical performance of Li–CO_2 batteries with the designed catalysts

Considering the attractive structural properties, the electrochemical performance of the Li–CO_2 batteries assembled with the prepared catalysts was evaluated. The cyclic voltammetry (CV) curves of the batteries based on Cu/NC catalysts were

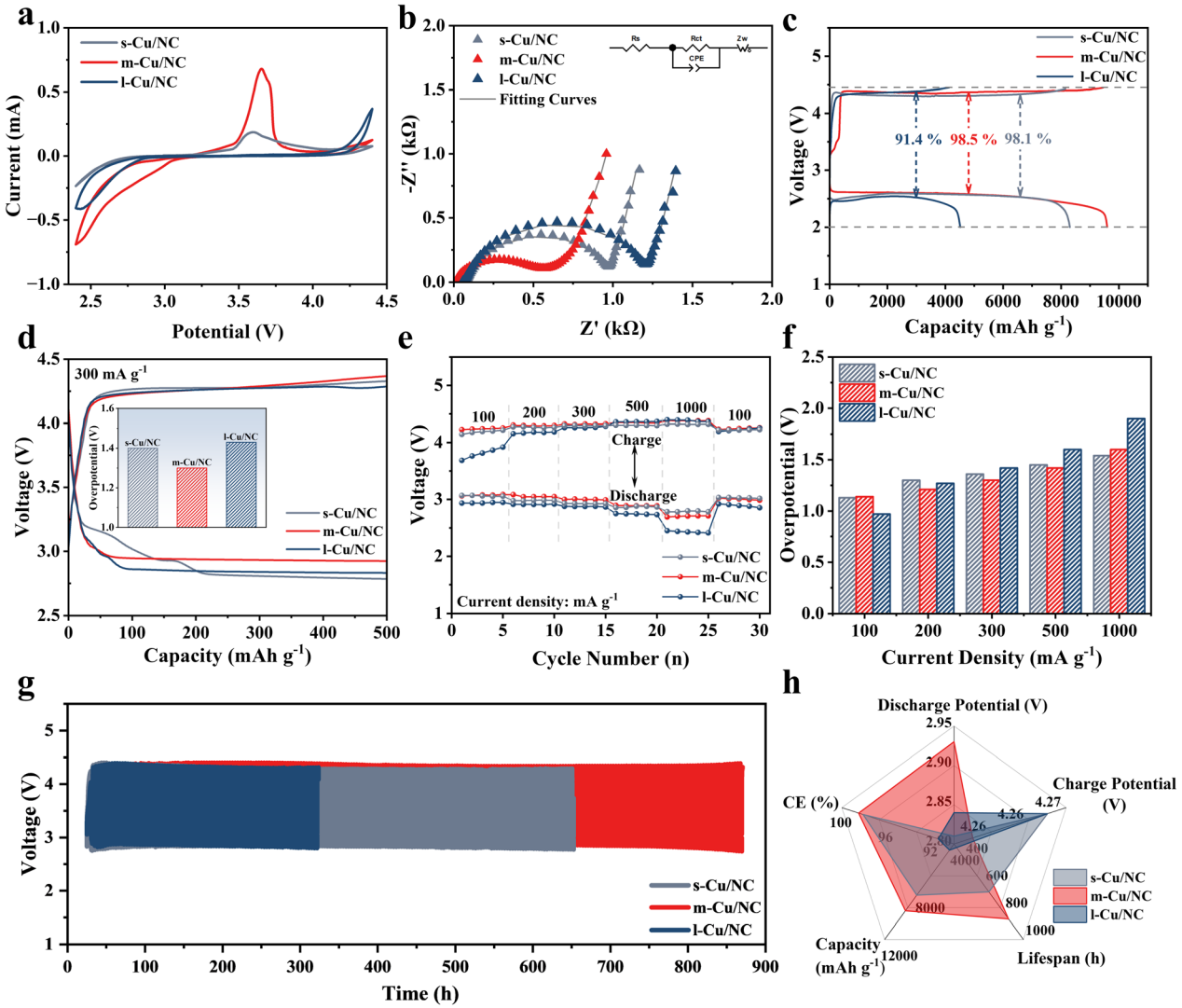

Fig. 3 (a) Cyclic voltammetry curve of the designed catalyst-based Li–CO_2 batteries under a CO_2 atmosphere. (b) Electrochemical impedance spectroscopy of the three samples for Li–CO_2 batteries. (c) Full discharge and charge curves of the three samples at 500 mA g^{-1}. (d) Cycle performance of the three samples at a limited capacity of 500 mA h g^{-1} at 300 mA g^{-1}. (e and f) Rate performances at different current densities. (g) Voltage–time curves of the three samples at 300 mA g^{-1} with a limited capacity of 500 mA h g^{-1}. (h) Electrochemical performance comparison of the three catalysts.

recorded at a scan rate of 0.1 mV s^{-1} over a voltage range of 2.4 V to 4.4 V. From Fig. 3a we can see that the battery with all the catalysts exhibits good activity in the CO_2 atmosphere and shows negligible capacity under the Ar atmosphere (Fig. S6), confirming the necessity of CO_2 as a reactant during redox reaction processes. The m-Cu/NC cathode exhibited more pronounced redox peaks at approximately 2.85 V (E_{c1}) and 3.65 V (E_{a1}),[6] corresponding to the formation and decomposition of the discharge product Li_2CO_3, respectively. The observed oxidation peak is lower than the conventional value of 3.8 V (*vs.* Li/Li^+), and the reduction peak is higher than the typical 2.8 V (*vs.* Li/Li^+), indicating that the m-Cu/NC catalyst effectively reduces the reaction energy barrier for both processes.[10] Compared to the s-Cu/NC and l-Cu/NC curves, m-Cu/NC exhibits the largest peak currents, indicating its superior activity, which may be ascribed to its uniform spherical structure and good synergistic effect between pyridine N and multi-active sites.[57] Linear sweep voltammetry (LSV) was employed to characterize the reaction kinetics of the investigated systems. As shown in Fig. S7, m-Cu/NC exhibits a significantly higher current density (0.60 mA g^{-1}) than s-Cu/NC (0.22 mA g^{-1}) and l-Cu/NC (0.24 mA g^{-1}), indicating its superior catalytic activity. This enhanced activity will contribute to improving the electrochemical reaction efficiency and accelerating reaction kinetics.[58]

Electrochemical impedance spectroscopy (EIS) was performed to investigate the charge transfer kinetics of each electrode.[59] As shown in Fig. 3b, according to the equivalent circuit fitting results, the R_{ct} value of m-Cu/NC was calculated to be 474.8 Ω, which is lower than those of s-Cu/NC (886 Ω) and l-Cu/

NC (1139 Ω). The reason for this may be the formed embedded electric field of Cu NPs through the metal–CN interface, resulting in ultrafast charge separation.[17] Additionally, the uniform spherical structure of m-Cu/NC can shorten the transfer path of Li^+ and thus reduce the R_{ct} value.[60]

Fig. 3c and S8 show the full discharge–charge curves and the related coulombic efficiency (CE) of the three catalysts tested at 500 mA g^{-1}, which reveal that the m-Cu/NC exhibits a superior specific discharge capacity of 9602 mA h g^{-1} with a higher CE (98.5%) than those of the counterparts (8297 mA h g^{-1} and 98.1% for s-Cu/NC and 4513 mA h g^{-1} and 91.4% for l-Cu/NC), and even superior to those previously reported (Fig. S9 and Table S1), suggesting its excellent reversibility. Additionally, the m-Cu/NC catalyst exhibits a higher energy efficiency (EE) value of 59.3% at 500 mA g^{-1} under full discharge/charge conditions than its counterparts (Fig. S10 and Table S2), demonstrating its favorable energy efficiency.[61–64] When tested at 300 mA g^{-1}, the m-Cu/NC-based battery displays a lower polarization voltage of 1.30 V (Fig. 3d), confirming the significant promotion of optimized structure and active sites for CO_2 transfer kinetics.[65,66]

To evaluate the rate capability, the catalysts were tested at various current densities. As shown in Fig. 3e and f, the m-Cu/NC catalyst exhibits the lowest overpotentials of 1.14, 1.21, 1.30, 1.42, and 1.60 V at 100, 200, 300, 500, and 1000 mA g^{-1}, respectively, compared to its counterparts, demonstrating its good rate capability across a wide range of current densities. Additionally, the long-term cycling stability of the assembled batteries was investigated at 300 mA g^{-1}. The overpotential of the m-Cu/NC cathode increased by only 0.60 V after cycling for over 850 h. However, s-Cu/NC and l-Cu/NC show limited cycle life of 652 h and 326 h, respectively. Furthermore, the battery tested at 500 mA g^{-1} also achieved long-term cycling stability (570 h, Fig. S11). The reason for such attractive performance may be attributed to the synergistic catalytic effect of multiple

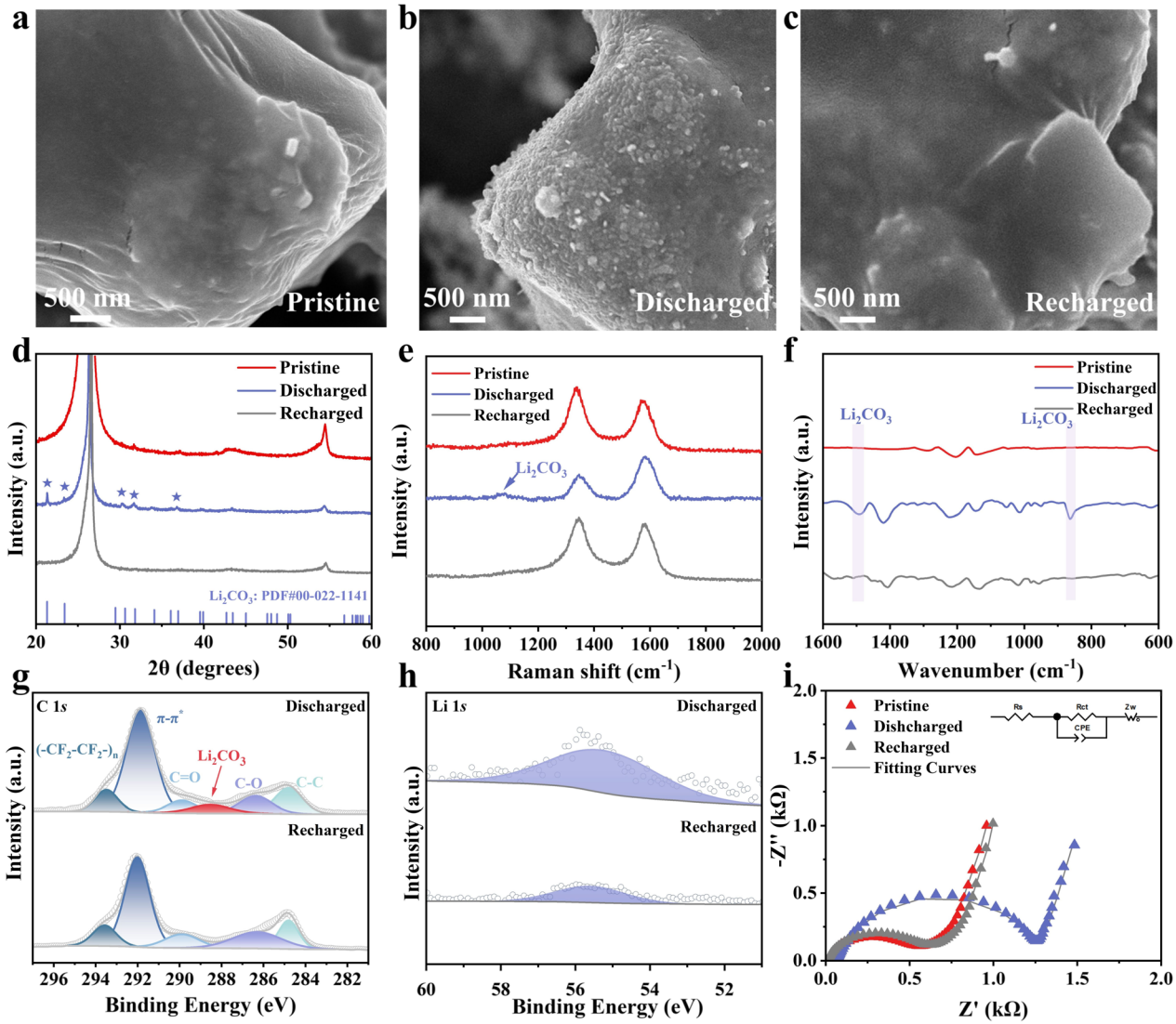

Fig. 4 Characterization of the m-Cu/NC cathode at different states. (a–c) SEM images of m-Cu/NC at the pristine, discharged, and recharged states, (d) XRD patterns, (e) Raman spectra, (f) FTIR, and (g and h) High resolution XPS spectra of C 1s and Li 1s of m-Cu/NC electrodes in the fully discharged state. (i) EIS spectra of m-Cu/NC at different states.

active sites (pyridine N, Cu NPs and Cu–N/O sites) and the NC structure, which can promote the mass transfer of CO_2 and Li^+, avoiding the clogging of discharge products on the electrode surface at high rates.[67] To further explore why the catalyst died after cycling, the battery was disassembled and it was found that the Li anode had completely lost its original metallic luster. When the disassembled m-Cu/NC catalyst was redeployed as the cathode with a fresh Li anode and the electrolyte, the reconstructed Li–CO_2 battery could still achieve 110 cycles (Fig. S12, at 300 mA g^{-1}) with an overvoltage of 1.58 V in the final cycle, confirming the stable catalytic performance of the catalyst.[68]

To elucidate the mechanism of the superior electrochemical performance of the m-Cu/NC-based Li–CO_2 battery, the cycled m-Cu/NC electrode at different states was analyzed using various techniques. SEM images (Fig. 4a and b) reveal that the discharged electrode surface is covered with uniformly distributed aggregates composed of small particles, compared to the pristine electrode. These aggregates completely disappear upon recharging (Fig. 4c). We infer that during the discharge process, the large specific surface area enhances CO_2 adsorption, where Cu NPs and Cu–N/O active sites adsorb and activate CO_2 molecules, which then combine with Li^+ to undergo reduction, forming Li_2CO_3 and C.[18] XRD analysis further supports this observation. As shown in Fig. 4d, distinct diffraction peaks matching the standard pattern of Li_2CO_3 appear on the discharged electrode, confirming Li_2CO_3 formation as the discharge product.[10–12] After recharging, these Li_2CO_3 peaks vanish, and the XRD profile reverts to resemble that of the pristine electrode, indicating decomposition of the discharge products. Additionally, Raman spectroscopy (Fig. 4e) and FTIR (Fig. 4f) detect characteristic peaks of Li_2CO_3 on the discharged electrode, which also disappear completely after recharging. The high-resolution XPS conducted on the electrode at different states (Fig. 4g and h) indicates that the C 1s spectrum shows a distinct peak at 288.5 eV after discharge, attributed to Li_2CO_3, which significantly diminishes after recharging. The other peaks at around 284.8, 286.6, 289.8, 291.9, and 293.5 eV were connected to C–C bonding, C–O bonding, C=O bonding, π–π bonding, and $(-CF_2-CF_2-)_n$, respectively.[69] Additionally, the peak at around 55.6 eV in the spectrum of Li 1s after the process of discharging can be attributed to the formation of Li in Li_2CO_3, which is significantly weakened when the battery is fully recharged, and the peak at 55.6 eV after the process of charging can be attributed to Li in a small amount of remaining lithium salt.[70] In addition, considering that the surface of the catalyst is covered with a wide bandgap insulating Li_2CO_3 layer, it will lead to an increase in the charge transfer impedance of the cathode during full discharge. EIS of the cycled m-Cu/NC cathode (Fig. 4i) suggests that the initial impedance value of the battery is approximately 474.8 Ω. After full discharge, the impedance increases to around 1167 Ω, which may be caused by the formation of insulating Li_2CO_3 and reduced carbon covering the catalyst and lithium surface, hindering electron transport.[71] However, after full recharging, the impedance decreases to 529.1 Ω, which can be ascribed to the effective decomposition of Li_2CO_3. This value nearly recovers to its initial state but is still slightly higher, likely due to the presence of trace amounts of undecomposed Li_2CO_3 and reduced carbon.[72] These results demonstrate the good reversibility of the battery. Therefore, it can be concluded that the existence of optimized N configuration, small Cu NPs and Cu–N/O promotes the decomposition of discharge products by reducing the decomposition energy barriers. Moreover, the larger specific surface area with enriched mesopores also provides space for the accumulation of discharge products, promoting the effective decomposition of discharge products and thus prolonging the cycle life of Li–CO_2 batteries.[67]

Conclusions

In summary, we demonstrate a rationally designed Cu–N/O multisite catalyst integrated with Cu nanoparticles (m-Cu/NC) synthesized *via* facile pyrolysis. This catalyst exhibits attractive bifunctional activity in Li–CO_2 batteries. The synergistic interplay between Cu–O and Cu–N coordination significantly enhances electron transfer kinetics, accelerating both CO_2 reduction and evolution reactions. The incorporated Cu NPs facilitate efficient electron transfer during the CO_2RR. Simultaneously, the N-doped carbon matrix further enhances catalytic activity for the CO_2RR and CO_2ER, concurrently optimizing electron transport and structural stability. Consequently, the m-Cu/NC-based Li–CO_2 battery achieves stable cycling for over 850 h at 300 mA g^{-1} with a low voltage gap of 1.30 V, outperforming existing Cu-based catalysts. This work highlights the promising potential of Cu-based materials in metal-air batteries and establishes new design principles for advanced bifunctional catalysts.

Author contributions

Y. X. and S. X. conceived the idea and wrote the manuscript. S. C. and Y. X. supervised the work and revised the manuscript. S. X. directed the project, prepared the samples, performed the electrochemical performance evaluation, and wrote the paper. G. H., T. Z., and L. Y. analysed part of the data and contributed to the preparation of the manuscript. F. H. revised the manuscript. All the authors discussed and analysed the results, and commented on the manuscript.

Conflicts of interest

The authors declare no conflict of interest.

Data availability

The data supporting this article have been included as part of the SI.

Catalyst synthesis, characterizations, and supporting Figures and Tables. See DOI: https://doi.org/10.1039/d5sc04645a.

Acknowledgements

This work was financially supported by the National Natural Science Foundation of China (52302210, 52425207,

U24A20566), Fundamental Research Funds for the Central Universities (buctrc202114, buctrc202104), and Open Cooperation Foundation of the Department of Chemical Science of Henan University.

References

1 Z. Chen, W. Zhou, S. Zhao, X. Lou and S. Chen, *Adv. Energy Mater.*, 2025, **15**, 2404108.
2 M. Zheng, Y. You and J. Lu, *Nat. Rev. Mater.*, 2025, **10**, 355.
3 S. Zhao, Q. Yu, S. Yang, S. Wan, J. Chen, H. Xu, X. Lou and S. Chen, *Nano Energy*, 2025, **138**, 110913.
4 S. Xiao, Y. Xiao, S. Hu, T. Zhang, G. He, J. Jing and S. Chen, *Energy Storage Mater.*, 2025, **75**, 104047.
5 Y. Liu, J. Zhang, T. Yan, G. Jin, J. Zhao, Y. Wang, X. Peng, H. Ma, J. Xu and D. Wang, *Energy Storage Mater.*, 2025, **76**, 104144.
6 W. Li, M. Zhang, X. Sun, C. Sheng, X. Mu, L. Wang, P. He and H. Zhou, *Nat. Commun.*, 2024, **15**, 803.
7 W. Li, X. Mu, S. Yang, D. Wang, Y. Wang, H. Zhou and P. He, *Angew. Chem., Int. Ed.*, 2025, **64**, e202422888.
8 Y. Cheng, Y. Wang, B. Chen, X. Han, F. He, C. He, W. Hu, G. Zhou and N. Zhao, *Adv. Mater.*, 2024, **36**, 2410704.
9 Q. Pan, X. Ma, H. Wang, Y. Shu, H. Liu, L. Yang, W. Li, J. Liu, Y. Wu, Y. Mao, J. Xie, G. Zou, H. Hou, W. Deng and X. Ji, *Adv. Mater.*, 2024, **36**, 2406905.
10 Y. Xing, Y. Yang, D. Li, M. Luo, N. Chen, Y. Ye, J. Qian, L. Li, D. Yang, F. Wu, R. Chen and S. Guo, *Adv. Mater.*, 2018, **30**, 1803124.
11 Y. Liu, S. Zhao, D. Wang, B. Chen, Z. Zhang, J. Sheng, X. Zhong, X. Zou, S. P. Jiang, G. Zhou and H.-M. Cheng, *ACS Nano*, 2022, **16**, 1523.
12 L. Liu, S. Shen, N. Zhao, H. Zhao, K. Wang, X. Cui, B. Wen, J. Wang, C. Xiao, X. Hu, Y. Su and S. Ding, *Adv. Mater.*, 2024, **36**, 2403229.
13 T. Chen, J. Cai, H. Wang, C. Gao, C. Yuan, K. Zhang, Y. Yu, W. Xiao, T. Luo and D. Xia, *Energy Environ. Sci.*, 2025, **18**, 853.
14 L. Liu, Y. Qin, K. Wang, H. Mao, H. Wu, W. Yu, D. Zhang, H. Zhao, H. Wang, J. Wang, C. Xiao, Y. Su and S. Ding, *Adv. Energy Mater.*, 2022, **12**, 2103681.
15 W. Ma, M. Gao, J. Ma, S. Liu, L. Yang, Y. Yang, X. Chen and T. Jian, *J. Energy Chem.*, 2025, **104**, 225.
16 J. Chen, X.-Y. Chen, Y. Liu, Y. Qiao, S.-Y. Guan, L. Li and S.-L. Chou, *Energy Environ. Sci.*, 2023, **16**, 792.
17 Y. Xu, H. Gong, L. Song, Y. Kong, C. Jiang, H. Xue, P. Li, X. Huang, J. He and T. Wang, *Mater. Today Energy*, 2022, **25**, 100967.
18 Y. Xu, C. Jiang, H. Gong, H. Xue, B. Gao, P. Li, K. Chang, X. Huang, T. Wang and J. He, *Nano Res.*, 2022, **15**, 4100.
19 Y. Xu, H. Gong, H. Ren, X. Fan, P. Li, T. Zhang, K. Chang, T. Wang and J. He, *Small*, 2022, **18**, 2203917.
20 T. Zhang, Z. Sun, S. Li, B. Wang, Y. Liu, R. Zhang and Z. Zhao, *Nat. Commun.*, 2022, **13**, 6996.
21 J. Ren, Z. Li, B. Qu, L. Meng, L. Bai, J. Sun, Z. Zhang, Y. Qu and L. Jing, *Adv. Mater.*, 2024, **36**, 2404392.
22 J.-X. Wu, P. P. Bag, Y.-T. Xu, L. Gong, C.-T. He, X.-M. Chen and J.-P. Zhang, *Adv. Mater.*, 2021, **33**, 2007368.
23 G. Arrachart, C. Carcel, P. Trens, J. J. E. Moreau and M. Wong Chi Man, *Chem.–Eur. J.*, 2009, **15**, 6279.
24 Y.-S. Jun, E. Z. Lee, X. Wang, W. H. Hong, G. D. Stucky and A. Thomas, *Adv. Funct. Mater.*, 2013, **23**, 3661.
25 B. Jürgens, E. Irran, J. Senker, P. Kroll, H. Müller and W. Schnick, *J. Am. Chem. Soc.*, 2003, **125**, 10288.
26 T. Zhou, X. Li, J. Zhao, L. Luo, Y. Wang, Z. Xiao, S. Hu, R. Wang, Z. Zhao, C. Liu, W. Wu, H. Li, Z. Zhang, L. Zhao, H. Yan and J. Zeng, *Nat. Mater.*, 2025, **24**, 891.
27 R. Duan, M. Xu, W. Qi, X. Hao, X. Xu, X. Liu and W. Liu, *Adv. Mater.*, 2025, **38**, 202501110.
28 M. Kuang, Q. Wang, P. Han and G. Zheng, *Adv. Energy Mater.*, 2017, **7**, 1700193.
29 M. Wang, K. Su, M. Zhang, X. Du and Z. Li, *ACS Sustainable Chem. Eng.*, 2021, **9**, 13324.
30 K. Wu, X. Chen, S. Liu, Y. Pan, W.-C. Cheong, W. Zhu, X. Cao, R. Shen, W. Chen, J. Luo, W. Yan, L. Zheng, Z. Chen, D. Wang, Q. Peng, C. Chen and Y. Li, *Nano Res.*, 2018, **11**, 6260.
31 X. Gong, J. Zhu, J. Li, R. Gao, Q. Zhou, Z. Zhang, H. Dou, L. Zhao, X. Sui, J. Cai, Y. Zhang, B. Liu, Y. Hu, A. Yu, S.-h. Sun, Z. Wang and Z. Chen, *Adv. Funct. Mater.*, 2021, **31**, 2008085.
32 H.-M. Wen, C. Liao, L. Li, A. Alsalme, Z. Alothman, R. Krishna, H. Wu, W. Zhou, J. Hu and B. Chen, *J. Mater. Chem. A*, 2019, **7**, 3128.
33 L. Peng, C.-T. Hung, S. Wang, X. Zhang, X. Zhu, Z. Zhao, C. Wang, Y. Tang, W. Li and D. Zhao, *J. Am. Chem. Soc.*, 2019, **141**, 7073.
34 Y. Wen, W.-H. Cheng, Y.-R. Wang, F.-C. Shen and Y.-Q. Lan, *Small*, 2024, **20**, 2307467.
35 H. Yu, A. Fisher, D. Cheng and D. Cao, *ACS Appl. Mater. Interfaces*, 2016, **8**, 21431.
36 Y. Zhou, Y. Wang, C. Fu, J. Zhou, Y. Song, S. Lin, S. Liang, S. Zhou and A. Pan, *Small*, 2024, **20**, 2405921.
37 Z. Pei, H. Li, Y. Huang, Q. Xue, Y. Huang, M. Zhu, Z. Wang and C. Zhi, *Energy Environ. Sci.*, 2017, **10**, 742.
38 R. Song, J. Han, S. Tian, D. Wang and D. Liu, *J. Power Sources*, 2025, **626**, 235763.
39 X. Huang, Y. Li, S. Xie, Q. Zhao, B. Zhang, Z. Zhang, H. Sheng and J. Zhao, *Angew. Chem., Int. Ed.*, 2024, **63**, e202403980.
40 Q. Hu, M. Li, J. Zhu, Z. Zhang, D. He, K. Zheng, Y. Wu, M. Fan, S. Zhu, W. Yan, J. Hu, J. Zhu, Q. Chen, X. Jiao and Y. Xie, *Nano Lett.*, 2024, **24**, 4610.
41 K. Liu, H. Shen, Z. Sun, Q. Zhou, G. Liu, Z. Sun, W. Chen, X. Gao and P. Chen, *Nat. Commun.*, 2025, **16**, 1203.
42 M. Ayiania, E. Weiss-Hortala, M. Smith, J.-S. McEwen and M. Garcia-Perez, *Carbon*, 2020, **167**, 559.
43 K. Yu, H. Wang, W. Yu, Z. Zhang and Z. Bian, *Chem. Eng. J.*, 2025, **514**, 163048.
44 B. Ipek, M. J. Wulfers, H. Kim, F. Göltl, I. Hermans, J. P. Smith, K. S. Booksh, C. M. Brown and R. F. Lobo, *ACS Catal.*, 2017, **7**, 4291.
45 Y. Yao, Y. Zhou, X. Liu, Y. Li, D. Wang, X. Chi, X. Wang, R. Zhao, H. Zhang, Y. Sun, Z.-Y. Yang, Y. Wei and Y.-M. Yan, *J. Mater. Chem. A*, 2022, **10**, 20914.

46 Y. Liu, W. Liu, M. Du, W. Li, H. Masuda and S. Kang, *J. Environ. Chem. Eng.*, 2024, **12**, 112291.
47 D. Tang, G. Ji, J. Wang, Z. Liang, W. Chen, H. Ji, J. Ma, S. Liu, Z. Zhuang and G. Zhou, *Adv. Mater.*, 2024, **36**, 2309722.
48 K. Jia, J. Ma, J. Wang, Z. Liang, G. Ji, Z. Piao, R. Gao, Y. Zhu, Z. Zhuang, G. Zhou and H. Cheng, *Adv. Mater.*, 2023, **35**, 2208034.
49 G. Zhu, C. Xi, Y. Liu, J. Zhu and X. Shen, *J. Mater. Chem. A*, 2015, **3**, 7591.
50 L. Zhang, J. Feng, R. Wang, L. Wu, X. Song, X. Jin, X. Tan, S. Jia, X. Ma, L. Jing, Q. Zhu, X. Kang, J. Zhang, X. Sun and B. Han, *J. Am. Chem. Soc.*, 2025, **147**, 713.
51 H. Chen, Z. Liu, Y. Xu, X. Yu, Y. Tao, Y. Li, X. Huang, J. He and T. Wang, *Chem. Sci.*, 2025, **16**, 4295.
52 Z. Zhang, F. Zhang, Z. Song and L. Zhang, *ACS Catal.*, 2025, **15**, 296.
53 Y. Xu, R. Xie, Q. Li, J. Feng, H. Luo, Q. Ye, Z. Guo, Y. Cao, M. Palma, G. Chai, M.-M. Titirici and C. R. Jones, *Small*, 2023, **19**, 2302795.
54 W.-B. Yu, M. Yi, H.-H. Fu, M.-J. Pei, Y. Liu, B.-M. Xu, Y. Li, W. Yan and J. Zhang, *ACS Appl. Nano Mater.*, 2023, **6**, 2928.
55 Y. Dai, Y. Gu and Y. Bu, *Appl. Surf. Sci.*, 2020, **500**, 144036.
56 Y. Liu, W. Liu, M. Du, W. Li, H. Masuda and S. Kang, *J. Environ. Chem. Eng.*, 2024, **12**, 112291.
57 R. Song, J. Han, S. Tian, D. Wang and D. Liu, *J. Power Sources*, 2025, **626**, 235763.
58 S. Hu, Y. Xiao, S. Wang, S. Xiao, F. Gong, L. Yang and S. Chen, *Adv. Energy Mater.*, 2025, **16**, 202501001.
59 Q. Deng, T. Miao, Z. Wang, Y. Xu and X. Fu, *Chem. Eng. J.*, 2019, **378**, 122139.
60 H. Zhang, J. Liu, Z. Xu, Y. Bu, T.-S. Wu, W.-M. Tu, Y.-L. Soo, C. Lin, Y. Zhu, Q. Lei, J. Yin and T. W. B. Lo, *ACS Catal.*, 2025, **15**, 8966.
61 B. Chen, D. Wang, J. Tan, Y. Liu, M. Jiao, B. Liu, N. Zhao, X. Zou, G. Zhou and H.-M. Cheng, *J. Am. Chem. Soc.*, 2022, **144**, 3106.
62 J. Zhou, X. Li, C. Yang, Y. Li, K. Guo, J. Cheng, D. Yuan, C. Song, J. Lu and B. Wang, *Adv. Mater.*, 2019, **31**, 1804439.
63 L. Qie, Y. Lin, J. W. Connell, J. Xu and L. Dai, *Angew. Chem., Int. Ed.*, 2017, **56**, 6970.
64 Y. Hou, J. Wang, L. Liu, Y. Liu, S. Chou, D. Shi, H. Liu, Y. Wu, W. Zhang and J. Chen, *Adv. Funct. Mater.*, 2017, **27**, 1700564.
65 F. Ye, L. Gong, Y. Long, S. N. Talapaneni, L. Zhang, Y. Xiao, D. Liu, C. Hu and L. Dai, *Adv. Energy Mater.*, 2021, **11**, 2101390.
66 Y. Yang, S. Louisia, S. Yu, J. Jin, I. Roh, C. Chen, M. V. Fonseca Guzman, J. Feijóo, P.-C. Chen, H. Wang, C. J. Pollock, X. Huang, Y.-T. Shao, C. Wang, D. A. Muller, H. D. Abruña and P. Yang, *Nature*, 2023, **614**, 262.
67 S. Hu, Y. Xiao, F. Gong, S. Xiao, W. Wu, Y. Yang, L. Hua and S. Chen, *J. Power Sources*, 2024, **624**, 235592.
68 X. Li, J. Zhang, G. Qi, J. Cheng and B. Wang, *Energy Storage Mater.*, 2021, **35**, 148.
69 Y. Liu, Z. Zhang, J. Tan, B. Chen, B. Lu, R. Mao, B. Liu, D. Wang, G. Zhou and H.-M. Cheng, *Nat. Commun.*, 2024, **15**, 2167.
70 X. Ma, W. Zhao, Q. Deng, X. Fu, L. Wu, W. Yan and Y. Yang, *J. Power Sources*, 2022, **535**, 231446.
71 Y. Zhu, Y. Wei, P. Li, S. Liu, J. Zhang, L. Tian, P. Gao, Y. Zhang, J. Li, D. Wang, Y. Shen and M. Wang, *J. Mater. Chem. A*, 2024, **12**, 5133.
72 B. Lu, Z. Min, X. Xiao, B. Wang, B. Chen, G. Lu, Y. Liu, R. Mao, Y. Song, X.-X. Zeng, Y. Sun, J. Yang and G. Zhou, *Adv. Mater.*, 2024, **36**, 2309264.